Analysis of Maneuvering Fish Fin Hydrodynamics Using an Immersed Boundary Method

Srinivas Ramakrishnan* and Rajat Mittal†
Department of Mechanical and Aerospace Engineering
George Washington University, Washington, DC

George V. Lauder‡
The Museum of Comparative Zoology, Harvard University, Cambridge, MA, USA

Meliha Bozkurttas§
Department of Mechanical and Aerospace Engineering
George Washington University, Washington, DC

A thorough understanding of the pectoral fin hydrodynamics of the bluegill sunfish (Lepomis macrochirus) provides insight that can be applied to the design of propulsors for autonomous underwater vehicles (AUVs). The pectoral fin represents a continuously deforming complex moving boundary problem. For the sunfish, both propulsion and maneuvering are entirely controlled by the pectoral fins. First, the kinematics of the fish fins and body are obtained experimentally through the use of high-speed, high resolution cameras. Then, simulations are carried out using a Cartesian grid based immersed boundary method that can handle unstructured deforming boundaries with the digitized kinematics as input. Here, we present a detailed analysis of the performance of the pectoral fins involved in a turning maneuver.

I. Introduction

Nature and evolution have combined to produce a multitude of efficient and successful control surfaces and propulsors (wings of birds, fish fins etc.). Biomimetics is a rapidly growing field that hopes to incorporate the best features of design found in nature into engineering systems. Any such endeavor starts with establishing a clear understanding of the reasons for the success of an evolutionary design. The bluegill sunfish is of particular interest for its ability perform a wide range of maneuvers and steady swimming using just its pectoral fins. This is probably the result of evolution to thrive in its natural habitat of small flowing streams. The ability to maneuver effectively in small spaces helps it successfully forage for food and evade prey.

Recently, the performance of the pectoral fins in steady swimming was studied in great detail using proper orthogonal decomposition (POD) by Bozkurttas.[1] This type of decomposition of fin motion is needed to systematically study the role of flexibility on its performance. This feature of the pectoral fin motion distinguishes it from other moving control surfaces such as flapping foils which undergo strictly rigid body motion. This inherent flexibility may be advantageous in the design of effective underwater propulsion systems.[2] Through the above mentioned study,[1] a great deal is now known about steady locomotion of bluegill sunfish.

However, there does not exist the same degree of understanding about other equally important modes of operation of the pectoral fin. The present study attempts to fill this void through an investigation of a yaw

*Postdoctoral Scientist.
†Professor, Senior AIAA Member.
‡Professor.
§Exa Corporation, Burlington, MA, USA.

turn maneuver executed by the bluegill sunfish.[3] This maneuver is executed by the sunfish in response to a stimulus (refer to Figure 1(a)). This mimics a typical evasive response of the sunfish in its natural habitat. Finally, we note that the present work is a part of an ongoing multi-disciplinary effort that aims to develop robust and efficient flexible fin based propulsion.[1,2,4]

II. Methodology

A. Experimental Methodology

Figure 1 shows different frames of the bluegill sunfish executing a maneuver from a ventral view. The motion of the sunfish pectoral fin and body are captured using multiple high speed video cameras simultaneously operating at 250 or more frames per second with a 1024×1024 resolution.[4,5] Then, at a particular time step, several points are digitized, nominally using 300 points per time step. This procedure is repeated for different timesteps at equally spaced time intervals spanning a fin beat. Thus, the kinematics of the fin motion are acquired for the simulation (see Figure 2).

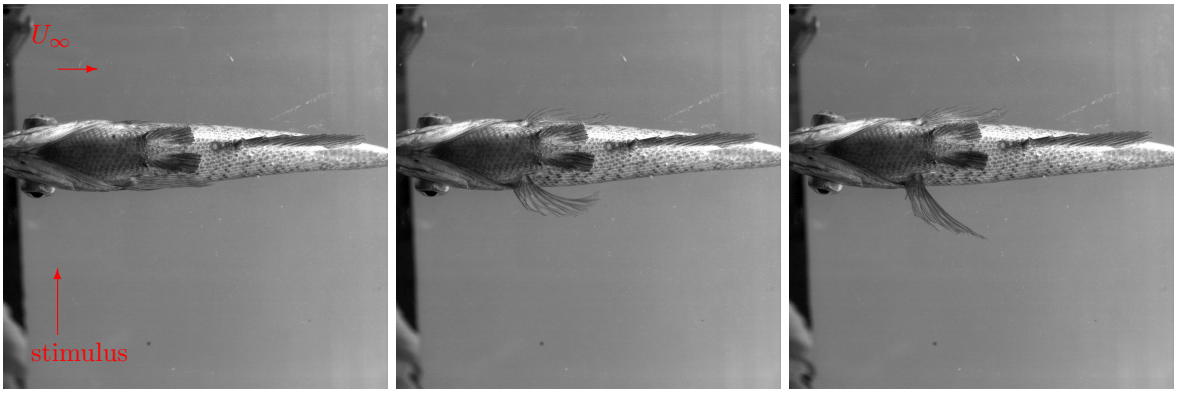

(a) (b) (c)

(d) (e) (f)

Figure 1. A bluegill sunfish during a maneuver: ventral (bottom) view.

B. Computational Methodology

We present a brief description of the Cartesian grid based immersed boundary method for moving boundaries starting with the governing equations. The three-dimensional unsteady, viscous incompressible Navier-Stokes equations are given as

$$\frac{\partial u_i}{\partial x_i} = 0 \tag{1}$$

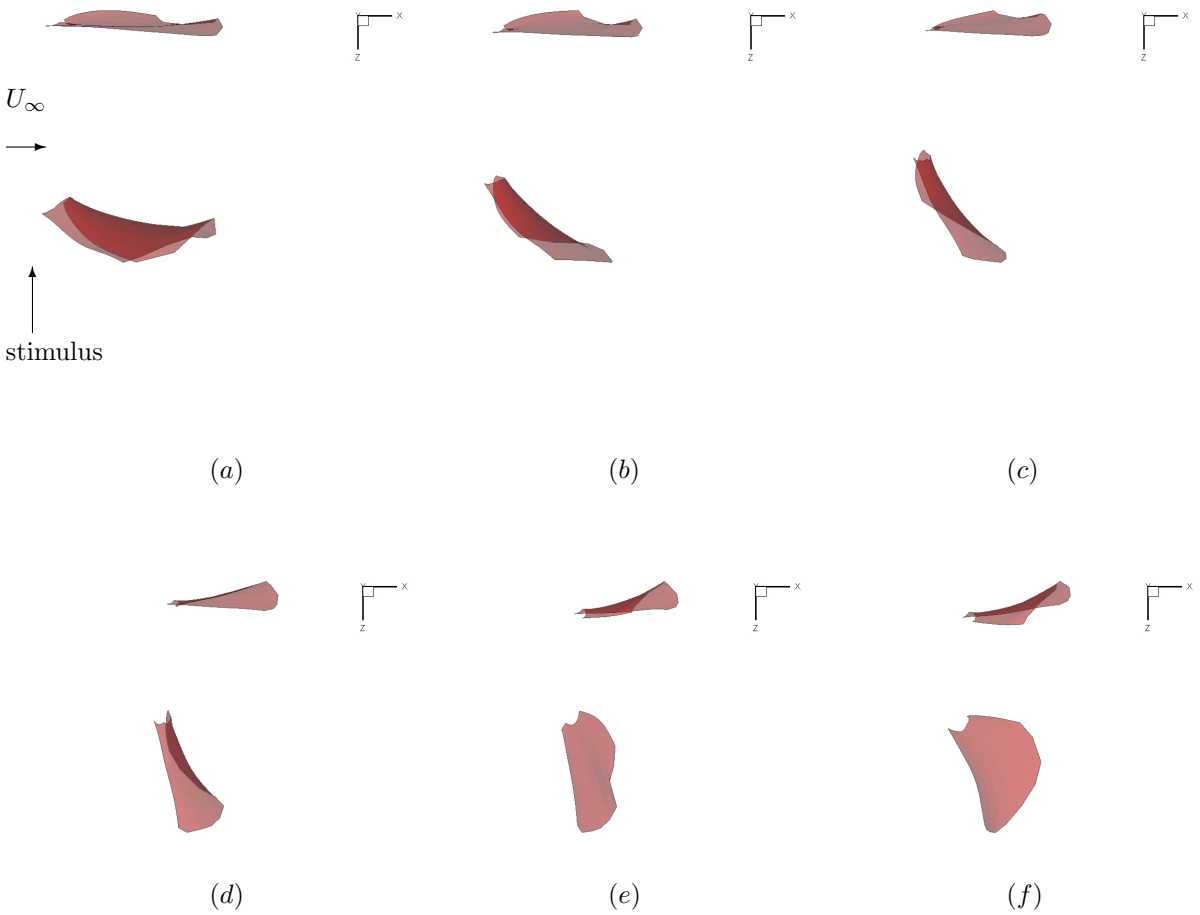

Figure 2. Kinematics of the pectoral fins input to the simulation.

$$\frac{\partial u_i}{\partial t} + \frac{\partial (u_i u_j)}{\partial x_j} = -\frac{1}{\rho}\frac{\partial p}{\partial x_i} + \nu \frac{\partial}{\partial x_j}\left(\frac{\partial u_i}{\partial x_j}\right) \tag{2}$$

where $i; j = 1, 2, 3$, u_i are the velocity component, p is the pressure, and ρ and ν are the fluid density and kinematic viscosity.

1. *Numerical Method*

The Navier-Stokes equations (2) are discretized using a cell-centered, collocated (non-staggered) arrangement of the primitive variables (u_i, p). In addition to the cell-center velocities (u_i), the face-center velocities, U_i, are computed. A second-order Adams-Bashforth scheme is employed for the convective terms while the diffusion terms are discretized using an implicit Crank-Nicolson scheme which eliminates the viscous stability constraint. The spatial derivatives are computed using a second-order accurate central difference scheme. The equations are integrated in time using the fractional step method.[6]In the first sub-step of this method a modified momentum equation is solved and an intermediate velocity u^* obtained. The second sub-step requires the solution of the pressure correction equation which is solved with the constraint that the final velocity u_i^{n+1} be divergence-free. This gives the following Poisson equation for the pressure correction and a Neumann boundary condition imposed on this pressure correction at all boundaries. This Poisson equation is solved with a highly efficient geometric multigrid method which employs a Gauss-Siedel line-SOR smoother. Once the pressure correction is obtained, the pressure and velocity are updated. These separately updated face-velocities satisfy discrete mass-conservation to machine accuracy and use of these velocities in estimating the non-linear convective flux leads to a more accurate and robust solution procedure. The advantage of separately computing the face-center velocities was initially proposed by Zang et al.[7] and discussed in the

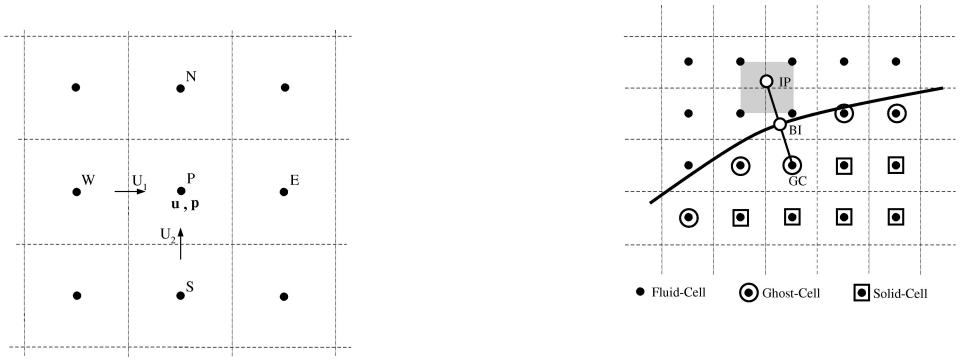

Figure 3. Schematic describing naming convention and location of velocity components (left) and the ghost-cell method (right).

context of the Cartesian grid methods in Ye et al.[8,9]

2. Immersed Boundary Treatment

The immersed boundary method used here employs a multi-dimensional ghost-cell methodology to impose the boundary conditions on the immersed boundary. The current solver is designed from the start for fast, efficient and accurate solution of flows with complex *three-dimensional*, *moving* boundaries. Also, the current method is a"sharp" interface method in that the boundary conditions on the immersed boundary are imposed at the precise location of the immersed body and there is no spurious spreading of boundary forcing into the fluid as what usually occurs with diffuse interface methods (See Mittal & Iaccarino[10] for details).

3. Geometric Representation of Immersed Boundary

The current method is designed to simulate flows over arbitrarily complex 2D and 3D immersed stationary and moving boundaries and the approach chosen to represent the boundary surface should be flexible enough so as not to limit the type of geometries that can be handled. A number of different approaches are available for representing the surface of the immersed boundary including level-sets ([11,12]), and unstructured surface grids. In the current solver we choose to represent the surface of the IB by a unstructured mesh with triangular elements. This approach is very well suited for the wide variety of flow engineering and biological configurations that we are interested and is compatible with the immersed boundary methodology used in the current solver.

4. Ghost-Cell Formulation

First, the surface mesh (see Figure 3) is embedded or immersed into the Cartesian grid. Next, a systematic procedure is developed to implement the ghost-cell methodology for such an immersed boundary. The method begins with identifying cells whose nodes are inside the solid boundary (termed "solid cells") and cells that are outside the body (termed "fluid cells"). Once the solid-fluid interface has been determined, the next step is to mark the so-called "ghost-cells". These are cells whose nodes are inside the solid but have at least one north, south, east or west neighbor in the fluid. The overall approach now is to determine an appropriate equation for these ghost cells that implicitly satisfies the imposed physical boundary condition on the immersed boundary in the vicinity of each ghost-cell. This is accomplished by extending a line segment from the node of these cells into the fluid to an "image-point" (denoted by IP) such that it intersects normal

to the immersed boundary and the boundary intercept (denoted by BI) lies midway between the ghost-node and the image-point. Next, the cells surrounding the IP are identified and bilinear interpolation is used to compute the value of generic variable ϕ at the image point as follows,

$$\phi_{IP} = \sum \beta_i \phi_i \tag{3}$$

where i extends over all the surrounding cells and β_i are the associated interpolation weights of these cells. Following this, the value of variable at the ghost-cell (denoted by GC) is computed by using a central-difference approximation along the normal probe which incorporates the prescribed boundary condition at the boundary intercept. Thus, for Dirichlet and Neumann boundary conditions, the formulas are:

$$\phi_{GC} = 2\phi_{BI} - \phi_{IP} \tag{4}$$

and

$$\phi_{GC} = \Delta l_p \left(\frac{\delta\phi}{\delta n}\right)_{BI} + \phi_{IP} \tag{5}$$

respectively where Δl_p is the total length of the normal line segment. Equations 4 and 5 can now be combined with Eq. 3 to give an implicit expression for the ghost-node values ie.

$$\phi_{GC} + \sum \beta_i \phi_i = 2\phi_{BI} \tag{6}$$

and

$$\phi_{GC} - \sum \beta_i \phi_i = \Delta l_p \left(\frac{\delta\phi}{\delta n}\right)_{BI} \tag{7}$$

respectively for these two types of boundary conditions. These equations are then solved in a fully coupled manner with the discretized governing equations 2 for the neighboring fluid cells along with the trivial equation $\phi = 0$ for the internal solid cells. Using this procedure, the boundary conditions are prescribed to second-order accuracy and this along with the second-order accurate discretization of the fluid cells leads to local and global second-order accuracy in the computations.

5. Boundary Motion

Boundary motion can be included into the above formulation with relative ease. In advancing the field equations from time level n to $n+1$ in the case of a moving boundary, the first step is to move from its current location to the new location. This is is accomplished by moving the nodes of the surface triangles with a known velocity. Thus we employ the following equation to update the coordinates (X_i) of the surface element vertices

$$\frac{X_i^{n+1} - X_i^n}{\Delta t} = V_i^{n+1} \tag{8}$$

where V_i is the vertex velocity. The vertex velocity can either be prescribed or it can be computed from a dynamical equation if the body motion is coupled to the fluid. The next step is to determine the ghost-cells for this new immersed boundary location and recompute the body-intercepts, image-points and associated weights βs. Subsequently, the flow equations which are written in Eulerian form are advanced in time. The general framework described above can therefore be considered as Eulerian-Lagrangian, wherein the immersed boundaries are explicitly tracked as surfaces in a Lagrangian mode, while the flow computations are performed on a fixed Eulerian mesh. Additional details regarding the immersed boundary methodology may be found in Dong *et al*,[13] Bozkurttas[1] and Mittal *et. al.*[9]

III. Simulation of Yaw Turn Maneuver

A. Computational Setup

The pectoral fins and an idealized body, immersed in the computational grid, are shown in Figure 4. The fins are modeled as deforming membranes while the body is treated as rigid body undergoing general motion.

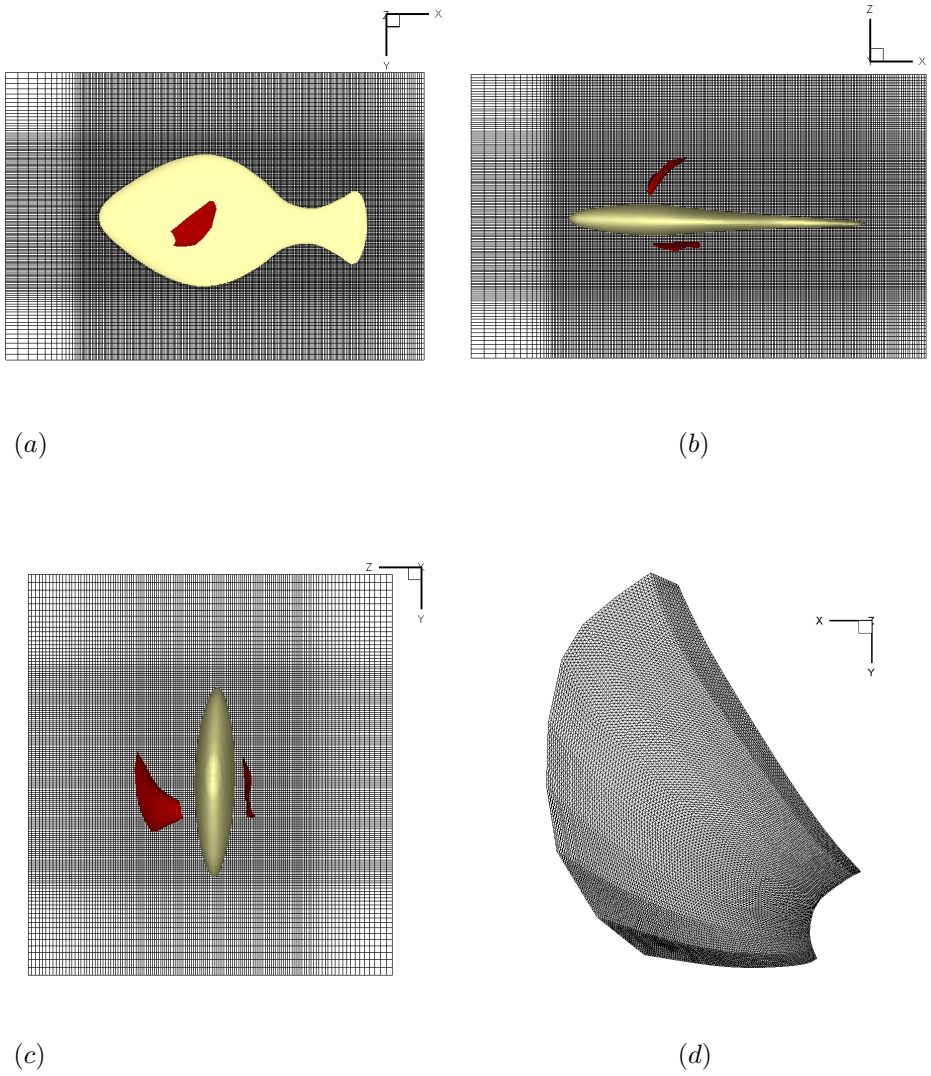

Figure 4. Cartesian grid and unstructured mesh employed for yaw maneuver : (a) $x-y$ plane section (4.8 million grid points); (b) $x-z$ plane section ; (c) $y-z$ plane section; (d) Unstructured Surface Mesh (Pectoral Fin, nodes= 10000, elements= 19602)

The nominal grid size used in the current simulation is $241 \times 145 \times 145$ (see Figure 4). The Reynolds number is defined as $Re = U_\infty L_s/\nu$, where U_∞, L_s, and ν are the freestream velocity, spanwise fin length, and the kinematic viscosity of water ($\nu = 1.007 \times 10^{-6} m^2 s^{-1}$ at room temperature (20 degrees Celsius)). The domain size employed for the maneuver is $7.5L_s \times 5L_s \times 5L_s$. The Reynolds number for the turning maneuver is approximately 3500 based on spanwise fin length and a freestream velocity of 0.5 body lengths per second. The boundary conditions on the domain are freestream on the left, outflow on the right while the remaining boundaries employ slip or symmetry boundary conditions (see Figure 4(a)). Finally, the fin surface and fish body are considered no slip boundaries.

B. Computational Results

Figure 5 shows the comparison of the time history of force coefficients developed on the strongside and weakside fin. The force coefficients are defined as,

$$C_d = \frac{2F_x}{\rho U_\infty^2 A_{fin}}, \quad C_l = \frac{2F_y}{\rho U_\infty^2 A_{fin}}, \text{ and, } \quad C_z = \frac{2F_z}{\rho U_\infty^2 A_{fin}}, \tag{9}$$

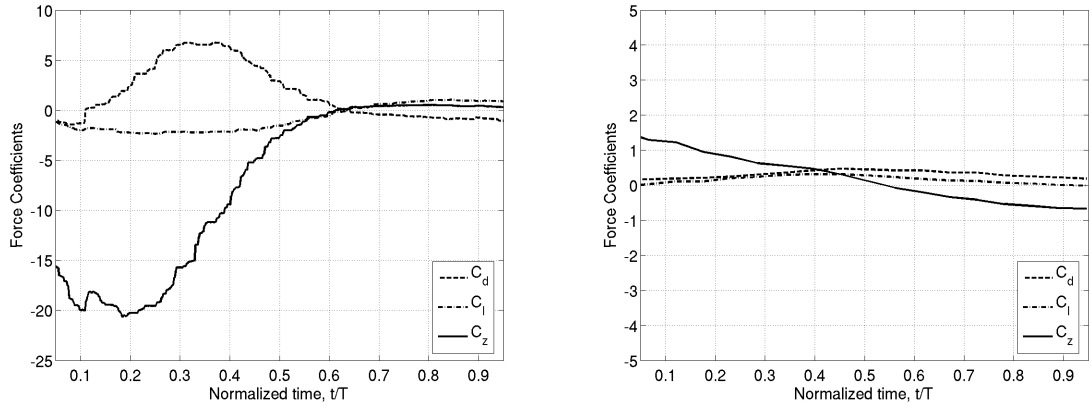

Figure 5. Comparison of time variation of force coefficients: (a)strongside; (b) weakside.

where F_x, F_y, and F_z are the forces respectively in the streamwise, vertical, and spanwise directions, A_{fin} is the nominal fin area, and ρ is the density of the fluid. Clearly, the magnitude of the forces on the weakside are an order of magnitude lower (see Figure 5(b)). This is consistent with the observation that the spatial and temporal kinematics of the strong side fin show greater variation with respect to the weak side fin (refer to Figures 1 and 2). Therefore, it comes as no surprise that the dynamics of the strongside pectoral fin dominate the maneuver. Thus, we focus exclusively on the strongside fin performance in our discussion hereafter.

Figure 6 shows the evolution of the wake structure emanating as result of the strongside fin kinematics from two vantage points: lateral (Figure 6 (a,c,e)) and dorsal (Figure 6 (b,d,f)). The strong fin is successful in generating a strong vortex ring during the outstroke by sweeping the entire planform in opposition to the freestream. This motion simultaneously produces a large force in the streamwise (C_d) direction while generating significant lateral (C_z) thrust (see Figure 5(a)). The lateral thrust is a direct result of the reaction to the strong lateral jet flow away from the body (see Figure 7). The evolving vortex ring, clearly seen in Figure 6 (d) and (f), continues to be oriented nearly parallel to the fish body. Consequently, the lateral jet orientation ensures that the maximum lateral force continues to act normal to the fish body for the duration of the maneuver. Meanwhile, the forces directed vertically (C_l) are negligible compared to C_d and C_z.

Importantly, the vortex ring and the associated lateral jet, shown in Figure 6 and 7, have also been observed in experimental visualization.[3] The peak lateral velocity is found to be greater than 3 times the freestream velocity. Consequently, the lateral forces developed are several times that observed in forward thrust for the steady swimming case.[1] Preliminary estimates suggest this factor may be as high as 4. This factor is in reasonable agreement with the forces measured experimentally.[3]

Returning to Figure 5(a)), we note that the C_z peak is reached between $t/T = 0.15$ and $t/T = 0.3$. Shortly after, the C_d peak occurs between $t/T = 0.3$ and $t/T = 0.4$. As expected, the first priority in the maneuver is to evade the stimulus (prey in the wild) by quickly generating a strong lateral force (maximum occurs at $t/T \approx 0.2$). Thereafter, the drag force developed in the streamwise direction is likely used to modulate the direction of the resultant force as the sunfish turns away from the stimulus. Here, the inherent flexibility of the pectoral fin structure and the ability to alter planform area is likely to be very useful.

Finally, we attempt to identify the source of the principal force production by dividing the strongside pectoral fin into dorsal and ventral halves (see Figure 8). A comparison of the force histories obtained using just the dorsal and ventral halves is shown in Figure 9. It is found that the peak lateral thrust developed by the dorsal part is approximately 70% of the lateral force as opposed to 30% for the ventral portion (see Figure 9(c)). Meanwhile, the streamwise force magnitudes are comparable except that the ventral portion appears to contribute minimally in thrust production, if any (see Figure 9(a)). And finally, the ventral and dorsal portions appear to produce vertical forces that are in opposite directions, respectively. This is consistent with the minimal vertical forces observed with the full pectoral fin (see Figure 5 (a)). As a result, the dorsal C_l is often times greater than the full fin C_l over the course of the maneuver (see Figure 9(b)). Overall, while the dorsal portion contributes to the majority of lateral force production, the ratio of dorsal

to ventral contribution appears to be more equitable than the steady swimming case discussed earlier.[1]

IV. Conclusions

A successful simulation of the yaw turn maneuver is performed using a Cartesian grid based immersed boundary method.[9,10,13] The strong lateral jet produced by the strongside fin motion, observed in the experiments,[3] is reproduced in the simulation. The lateral force, as expected, is significantly larger compared with steady swimming suggesting a wider operational envelope for the pectoral fin. The bluegill sunfish appears to actively employ a larger portion of the fin in executing the maneuver likely due to the increased force requirements when compared to steady swimming.[1] Even so, the dorsal half of the fin still appears to supply a majority of the lateral force.

V. Acknowledgments

This work is supported under ONR-MURI Grant N00014-03-1-0897 monitored by Dr. Thomas McKenna.

References

[1]Bozkurttas, M., *Hydrodynamic Performance of Fish Pectoral Fins with Application to Autonomous Underwater Vehicles*, Ph.D. thesis, George Washington University, 2007.

[2]Bozkurttas, M., Dong, H., Mittal, R., Tangorra, J., Hunter, I., Lauder, G. V., and Madden, P., "CFD based Analysis and Design of Biomimetic Flexible Propulsors for Autonomous Underwater Vehicles," *37th AIAA Fluid Dynamics Conference and Exhibit*, 2007.

[3]Drucker, E. G. and Lauder, G. V., "Wake Dynamics and Fluid Forces of Turning Maneuvers in Sunfish," *J. Exp. Biol.*, Vol. 204, 2001, pp. 431–442.

[4]Mittal, R., Dong, H., Bozkurttas, M., and Lauder, G. V., "Locomotion with Flexible Propulsors: II. Computational Modeling of Pectoral Fin Swimming in Sunfish," *Bioinspiration and Biomimetics*, Vol. 1, 2006, pp. S25–S34.

[5]Lauder, G. V., Madden, P. G. A., Mittal, R., and Dong, H., "Locomotion with Flexible Propulsors: I. Experimental Analysis of Pectoral Fin Swimming in Sunfish," *Bioinspiration and Biomimetics*, Vol. 1, 2006, pp. S35–S41.

[6]Chorin, A. J., "A Numerical Method for Solving Incompressible Viscous Flow Problems," *J. Comp. Phys.*, Vol. 2, 1967.

[7]Zang, Y., Street, R. L., and Koseff, J. R., "A non-staggered grid, fractional step method for time-dependent incompressible Navier-Stokes equations in curvilinear coordinates," *Journal of computational physics*, Vol. 114, 18, 1994.

[8]Ye, T., Mittal, R., Udaykumar, H. S., and Shyy, W., "An accurate Cartesian grid method for simulation of viscous incompressible flows with complex immersed boundaries," *J. Comput. Phys.*, Vol. 156, 1999, pp. 209–240.

[9]Mittal, R., Dong, H., Bozkurttas, M., Najjar, F., Vargas, A., and von Loebbecke, A., "A Versatile sharp interface immersed boundary method for incompressible flows with complex boundaries," *Journal of computational physics*, Vol. 227, 10, 2008, pp. 4825–4852.

[10]Mittal, R. and Iaccarino, G., "Immersed Boundary Methods," *Annu. Rev. Fluid Mech.*, Vol. 37, 2005, pp. 239–61.

[11]Osher, S. and Sethian, J. A., "Fronts Propagating with Curvature-Dependent Speed - Algorithms Based on Hamilton-Jacobi Formulations," *J. Comp. Phys.*, Vol. 79, 1988, pp. 12–49.

[12]Tran, L. B. and Udaykumar, H. S., "A particle-level set-based sharp interface cartesian grid method for impact, penetration, and void collapse," *J. Comp. Phys.*, Vol. 193, 2004, pp. 469–510.

[13]Dong, H., Mittal, R., and Najjar, F. M., "Wake Topology and Hydrodynamic Performance of Low-aspect-ratio Flapping Foils," *J. Fluid Mech..*, Vol. 566, 2006, pp. 309–343.

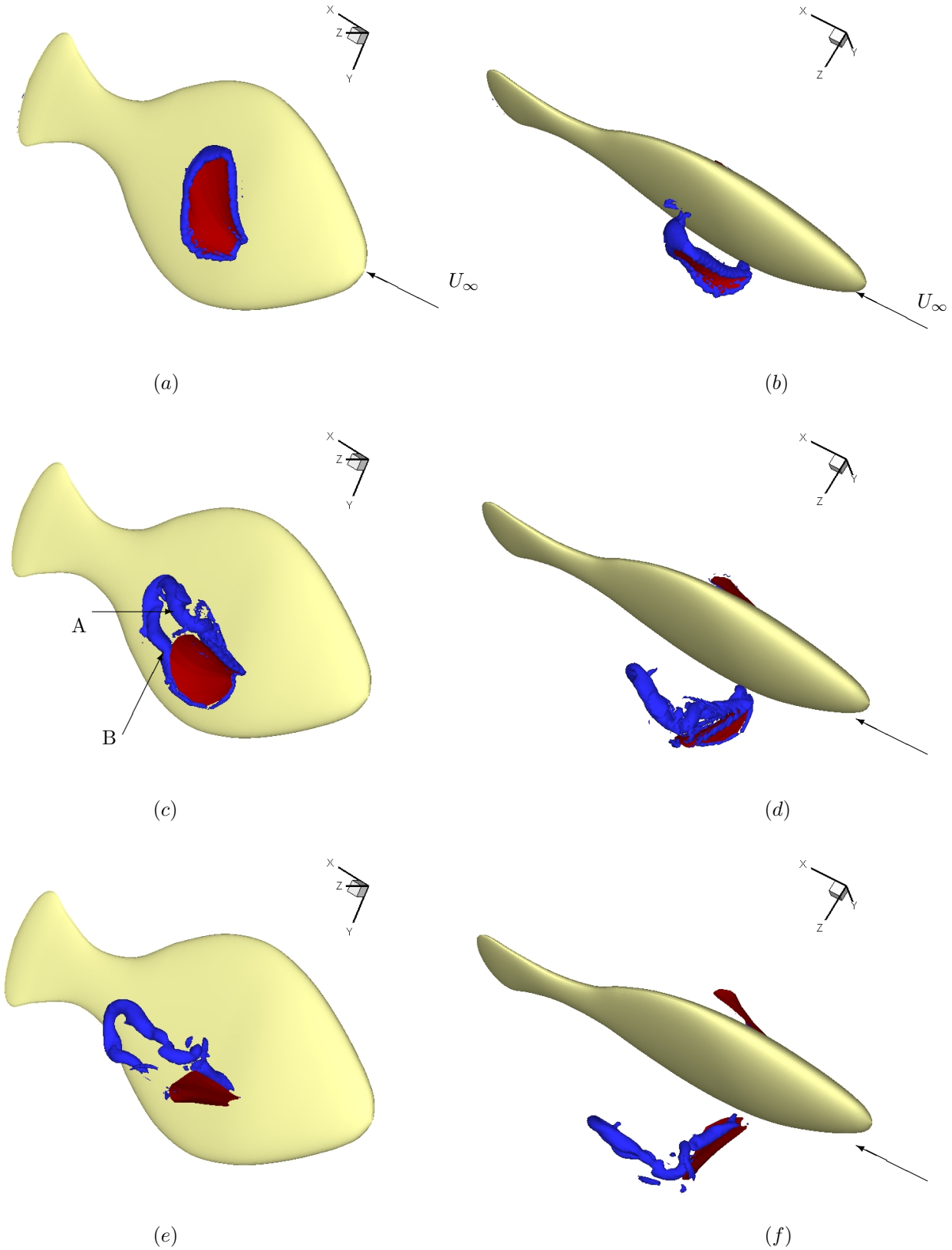

Figure 6. Formation of the vortex ring due to the strongside pectoral fin motion: (a), (c), and (e) are lateral views at $t/T = 0.22$, $t/T = 0.49$, and $t/T = 0.66$, respectively; (b), (d), and (f) are the corresponding dorsal views at $t/T = 0.22$, $t/T = 0.49$, and $t/T = 0.66$, respectively.

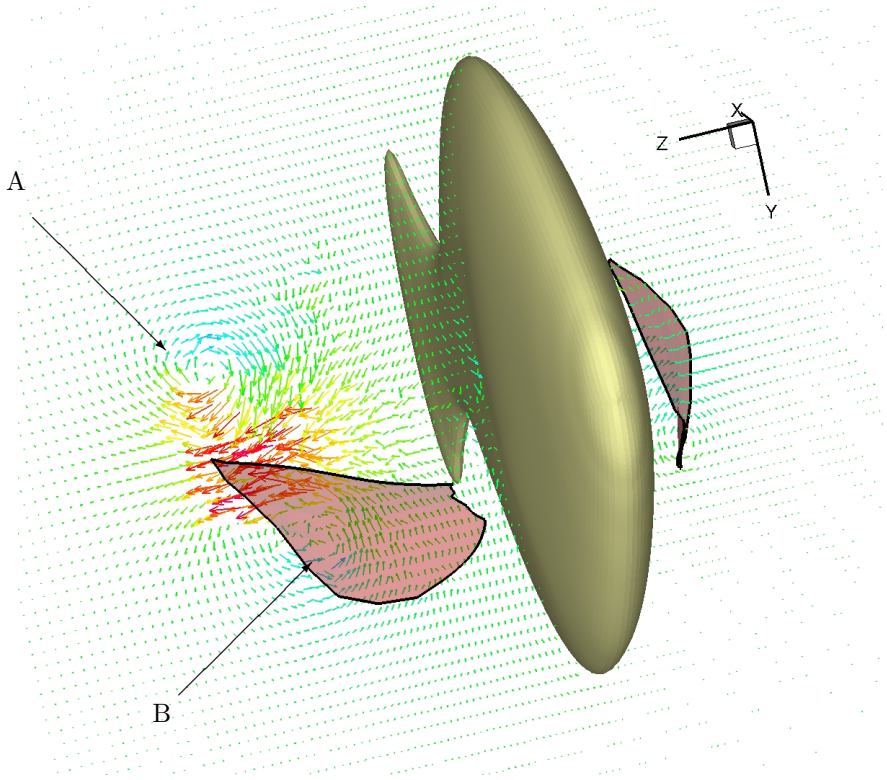

Figure 7. The strongside lateral jet associated with the vortex structures in Figure 6(c) at $t/T = 0.49$.

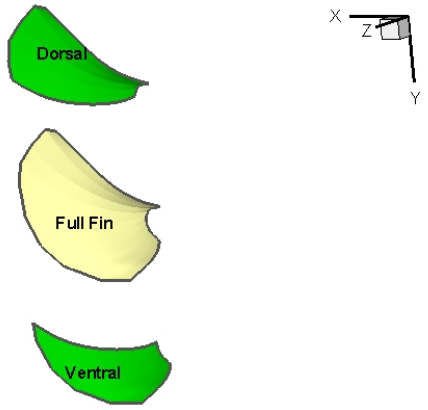

Figure 8. Illustration of sectioning of the strongside pectoral fin into ventral and dorsal halves.

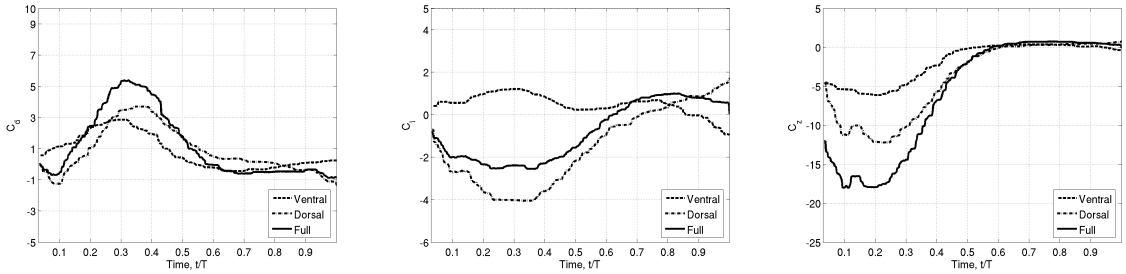

(a) (b) (c)

Figure 9. Comparison of forces produced on the dorsal and ventral halves of the strong side fin with respect to the full fin: (a) Streamwise Force; (b) Vertical Force; (c) Lateral Force.